

Measurement of Snowpack Density, Grain Size, and Black Carbon Concentration Using Time-domain Diffuse Optics

Connor HENLEY,^{1,2} Joseph L. HOLLMANN,² Colin R. MEYER,³ Ramesh RASKAR¹

¹*MIT Media Lab, Massachusetts Institute of Technology, 75 Amherst Street, Cambridge, MA, USA*

²*The Charles Stark Draper Laboratory, Inc., 555 Technology Square, Cambridge, MA, USA*

³*Thayer School of Engineering, Dartmouth College, 15 Thayer Drive, Hanover, NH, USA*

Correspondence: Connor Henley <co24401@mit.edu>

ABSTRACT. Diffuse optical spectroscopy (DOS) techniques aim to characterize scattering media by examining their optical response to laser illumination. Time-domain DOS methods involve illuminating the medium with a laser pulse and using a fast photodetector to measure the time-dependent intensity of light that exits the medium after multiple scattering events. While DOS research traditionally focused on characterizing biological tissues, we demonstrate that time-domain diffuse optical measurements can also be used to characterize snow. We introduce a model that predicts the time-dependent reflectance of a snowpack as a function of its density, grain size, and black carbon content, and we develop an algorithm that retrieves these properties from measurements at two wavelengths. To validate our approach, we use a two-wavelength lidar system and measure the time-dependent reflectance of snow samples with varying properties. Rather than measuring direct surface returns, our system captures photons that enter and exit the snow at different points, separated by a small distance (4-10cm). We find strong, linear correlations between our retrievals of density and black carbon concentration, and ground truth measurements. Although the correlation is not as strong, we also find that our method is capable of distinguishing between small and large grains.

INTRODUCTION

Snow is composed of transparent ice grains that absorb light very weakly at visible and near-infrared wavelengths (Warren, 2019). Because of this, photons that enter a snowpack will typically scatter many times off of a large number of ice grains before they either exit the medium or get absorbed. The study of snow optics has historically focused on the interaction of snow with *sunlight*, as understanding this interaction is essential to understanding snow cover's contribution to the Earth's climate (Henderson and others, 2018) and for forecasting snow melt (Painter and others, 2010), among other things. A key goal of snow optics has been to predict spectral albedo as a function of intrinsic snowpack properties—such as grain size, which determines the probability that a photon will be absorbed at each scattering event

(Wiscombe and Warren, 1980a), and the concentration of light absorbing particles such as dust, black carbon, or algae that are mixed into the snow (Wiscombe and Warren, 1980b; Skiles and others, 2018).

The development of accurate spectral albedo models has, in turn, led to the development of optical sensing methods that retrieve grain size (Nolin and Dozier, 2000; Gallet and others, 2009) and LAP concentrations (Zege and others, 2011; Painter and others, 2012) from spectral albedo measurements. These methods, while useful, have limitations. Snowpack albedo is largely independent of important properties such as snow density (Wiscombe and Warren, 1980a). Furthermore, spectral albedo measurements usually require passive illumination by sunlight, which precludes their use at night and for several months of the year in polar regions. Albedo models also assume steady-state illumination that is either collimated or diffuse. As such, they cannot fully model the optical response of snowpack to the focused, time-modulated illumination employed by lidar systems.

Over the past few decades, in parallel with advances in snow optics, the biomedical optics community has developed a suite of techniques for characterizing biological tissue, which, like snow, is also a highly scattering medium. Collectively, these methods are referred to under the umbrella term of *diffuse optical spectroscopy* (DOS) (Durduran and others, 2010), which refers to the fact that the propagation of photons within the scattering medium is modeled using the *diffusion approximation* to the radiative transfer equation (Welch and van Gemert, 1995), and to the fact that multi-wavelength illumination is frequently used (although this is not required). In DOS techniques the tissue is probed with a focused laser source that can be time-modulated, frequency-modulated, or continuous-wave. Measurements of the tissue's optical response are then used to estimate its optical properties, such as the tissue's absorption coefficient or effective scattering coefficient. These optical properties, in turn, can be related to clinically useful properties of the tissue such as blood oxygenation (Sevick and others, 1991), organelle size (Li and others, 2008), and the concentrations of water, lipids, and collagen (Quarto and others, 2014).

Because snow is also a highly scattering medium, many of the results from diffuse optical spectroscopy can be adapted to the characterization of snowpack properties. Despite this, the adoption of diffuse optics concepts in the snow sensing community has been limited. Várnai and Cahalan (2007) proposed that the spatial spread of diffused laser light could be used to determine snow and sea ice thickness. Smith and others (2018) noted that the multiple scattering of laser light within a snowpack should result in biases in lidar altimetry measurements. They used a combination of diffusion theory and Monte-carlo modeling to assess the dependence of this multiple scattering bias on grain size, black carbon concentration, and the choice of surface height retrieval algorithm. Fair and others (2022) experimentally confirmed the predictions of Smith and others (2018) by comparing biases in the snow surface heights retrieved by IceSat-2 and by the 532 nm and 1064 nm beams on the Airborne Topographic Mapper. As far as we are aware, prior to this work, the only direct application of DOS techniques to retrieve bulk snowpack properties was made by Allgaier and Smith (2022). In their work, the snow was illuminated with continuous-wave laser sources at two different wavelengths, and a smartphone camera was used to take images of the spatially resolved, steady-state intensity of light that exited the snowpack after diffusing within the snow. From these smartphone images, along with an independent *in situ* measurement of the snow's density, the authors were able to retrieve the absorption and effective scattering coefficients of the snowpack, as well as an estimate of the concentration of black carbon within it. In Ackermann and others (2006), and in a separate work by Allgaier and others

(2022), time-domain diffuse optical measurements were used to estimate the absorption and scattering coefficients of *glacier ice*, which is optically similar to snow when it is rich in air bubbles.

In this work we introduce what is, to our knowledge, the first method for characterizing the bulk properties of *snow* that is based on *time-domain* diffuse optical measurements. Our instrument is effectively a photon-counting lidar system that consists of two pulsed lasers with different wavelengths (one red, one near-infrared), and a single-photon avalanche diode (SPAD) receiver. Rather than measuring surface returns, which might be used for altimetry, we measure photons that enter the snowpack at a single point on the surface and exit at a second surface point that is displaced from the point of entry by a small distance (4-10 cm). Through a series of proof-of-principle experiments, we show that our method is capable of retrieving the snowpack density (through the ice volume fraction), grain size, and the concentration of light absorbing particles, in a non-invasive way. As far as we are aware, ours is the first method to estimate snowpack *density* using non-invasive optical reflectance measurements. Although our system uses the same components as a photon-counting lidar, our measurements are effectively *in situ*, as the instrument is always placed within a meter of the snow surface. However, by demonstrating that important bulk snowpack properties can be retrieved from time-domain measurements of multiply scattered photons, we hope that our work will motivate the future development of techniques that retrieve snowpack properties from remote lidar measurements. We also believe that time-domain diffuse optical measurements, in general, represent a new frontier for studying the optical properties of snow.

METHODS

Diffusion Model

The propagation of a laser pulse inside a scattering medium is described by the time-dependent radiative transfer equation (Welch and van Gemert, 1995), which models the flow of *radiance* ($\text{W} \cdot \text{m}^{-2} \cdot \text{sr}^{-1}$) within a medium as a function of space and time. The scattering medium is described by a scattering coefficient μ_s (m^{-1}), a scattering phase function, an absorption coefficient μ_a (m^{-1}), and the speed of light within the medium c_* (m/s).

Under the *diffusion approximation* to the radiative transfer equation, photons are modeled as particles that “diffuse” through a scattering medium via random walks. This approximation accurately describes situations for which the distance scales considered are much larger than the mean free path of photons within the medium ($= (\mu_a + \mu_s)^{-1}$), and photons are typically scattered many times before they are absorbed ($\mu_s \gg \mu_a$) (Welch and van Gemert, 1995). The photon diffusion equation can be written as follows:

$$\frac{1}{c_*} \frac{\partial}{\partial t} \phi(\mathbf{r}, t) - D \nabla^2 \phi(\mathbf{r}, t) + \mu_a \phi(\mathbf{r}, t) = S(\mathbf{r}, t). \quad (1)$$

A derivation of the photon diffusion equation can be found in Haskell and others (1994). Unlike the time-dependent radiative transfer equation, which models the time-evolution of a five-dimensional radiance field, the photon diffusion equation models the lower dimensional quantity of *photon fluence* $\phi(\mathbf{r}, t)$ ($\text{W} \cdot \text{m}^{-2}$), which is the integral of radiance over all directions. Here $D = 3 [\mu_a + (1 - g)\mu_s]^{-1}$ is the diffusion constant

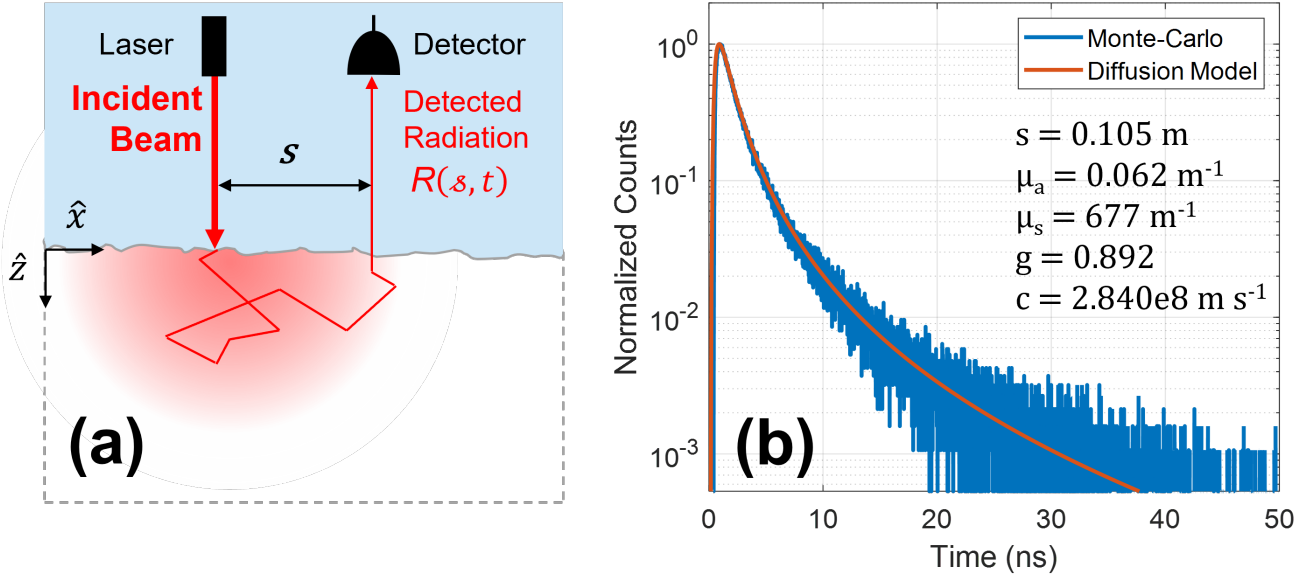


Fig. 1. (a) Illustration of the measurement geometry employed in this work. A point on the snow surface is illuminated by a laser pulse at time $t = 0$. A detector observes the time-dependent intensity of light that exits the snow at distance s from the laser spot. (b) Comparison of time-dependent intensity predicted by our model (Eq. 4), to photon time-of-flight measurements generated using a Monte-carlo simulation of a scattering medium with the same properties. Both curves are normalized to their respective peaks.

and g is the anisotropy factor of the scattering phase function, which can take values between -1 and 1 depending on whether the medium is primarily backward scattering ($g < 0$) or forward scattering ($g > 0$). The variable S represents an isotropic source term.

Crucially, the photon diffusion equation permits analytical solutions when the geometry of the scattering medium is sufficiently simple. We consider the scenario depicted in Fig. 1(a). Here, the medium is assumed to be semi-infinite and homogeneous. The medium's surface is illuminated by a pulsed, pencil-beam source at time $t = 0$, and a detector observes the time-dependent intensity of light that exits the medium at a second point that is displaced from the point of illumination by a small distance s . Kienle and Patterson (1997) showed that, in this scenario, Eq. 1 can be accurately solved by imposing an *extrapolated boundary condition*, which requires that photon fluence goes to zero along a planar boundary that lies just above the medium's surface. This yields the following expression for photon fluence inside the medium:

$$\phi(s, z, t) = \frac{c_*}{(4\pi D c_* t)^{3/2}} \exp(-\mu_a c t) \left\{ \exp \left[-\frac{(z - z_0)^2 + s^2}{4 D c_* t} \right] - \exp \left[-\frac{(z + z_0 + 2z_b)^2 + s^2}{4 D c_* t} \right] \right\}. \quad (2)$$

Here z denotes the distance from the surface, going down; $z_0 = [\mu_a + (1 - g)\mu_s]^{-1}$ is the transport mean free path of photons within the medium; and z_b denotes the height of the extrapolated boundary. Haskell and others (1994) proposed a value of $z_b = \frac{1+R_{eff}}{1-R_{eff}} 2D$, where R_{eff} is the fraction of photons that are internally reflected at the interface between the scattering medium and the external (non-scattering) medium due to a refractive index mismatch. Because our ultimate goal is to model the time-dependent optical response of a snowpack, and because the snow-air boundary of a typical snowpack is not a dielectric

interface at optical wavelengths, we assume for this work that $R_{eff} = 0$ and hence, $z_b = 2D$.

From Eq. 2, we compute the time dependent radiosity ($\text{W} \cdot \text{m}^{-2}$) that exits the surface at position s using Fick's Law (Kienle and Patterson, 1997)

$$J(s, t) = -D \nabla \phi(s, z, t) \cdot (-\hat{z})|_{z=0}. \quad (3)$$

The reflected flux R measured by a detector that observes the medium's surface from a distance can then be described using the following expression:

$$R(s, t) = \frac{\alpha c_*}{3(2\pi)^{3/2}} \frac{z_0^2}{(2Dc_*t)^{5/2}} \exp\left(-\mu_a c_* t - \frac{s^2 + z_0^2}{4Dc_*t}\right) \left[1 + \frac{7}{3} \exp\left(-\frac{10z_0^2}{9Dc_*t}\right)\right], \quad (4)$$

where α is a constant that encapsulates instrumental parameters such as transmitted laser power, detection efficiency, and the detector's etendue. We note that we have made liberal use of the substitutions $D = z_0/3$ and $z_b = 2z_0/3$. In deriving Eq. 4, we also assumed that the surface could be accurately described as a Lambertian emitter, which means that the radiance emitted by the surface is independent of the emission angle. Previous work has relaxed this assumption (Kienle and Patterson, 1997). We found that doing so produced nearly identical results when describing a nadir-pointing detector, but added significant complexity to the model. For this reason, we elected to use Eq. 4.

In Fig. 1(b) we compare the time-dependent intensity predicted by Eq. 4 to simulated photon time-of-flight measurements generated using a Monte-carlo simulation (Henley, 2020). The modeled results match the simulation very closely. In general, models derived from the diffusion approximation to the radiative transfer equation accurately describe the measurements of photons that arrive at later times ($c_*t \gg z_0$) and larger distances from the laser spot ($s \gg z_0$), as these photons have scattered many times before exiting the medium.

Snow Scattering Model

Our measurement model, defined in Eq. 4, is expressed in terms of three phenomenological parameters—the absorption coefficient μ_a , the effective scattering coefficient $\mu'_s = (1 - g)\mu_s$, and the speed of light in the medium c_* . As is often done when modeling snow albedo (Wiscombe and Warren, 1980a), we assume the snowpack can be modeled as a monodispersion of spherical ice grains. This assumption allows us to use a Mie scattering model to define μ_a , μ'_s , and c_* in terms of three physically meaningful snowpack parameters— v_* , the fraction of the snowpack volume that is occupied by ice; r_* (m), the grain radius; and C_{bc} (kg/kg), the mass mixing ratio of black carbon in the snowpack. We note that the ice volume fraction v_* is readily converted to snowpack density ρ_* (kg/m^3) via the expression $\rho_* = v_*\rho_{ice} + (1 - v_*)\rho_{air} \approx v_*\rho_{ice}$, where ρ_{ice} and ρ_{air} are the bulk densities of ice and air, respectively.

Clean Snowpack

For a snowpack that contains optically insignificant concentrations of light absorbing particles, the scattering and absorption coefficients can be written entirely as functions of v_* and r_* . We use Mie codes (Sumlin and others, 2018) to compute the scattering efficiency Q_s , the absorption efficiency Q_a , and the

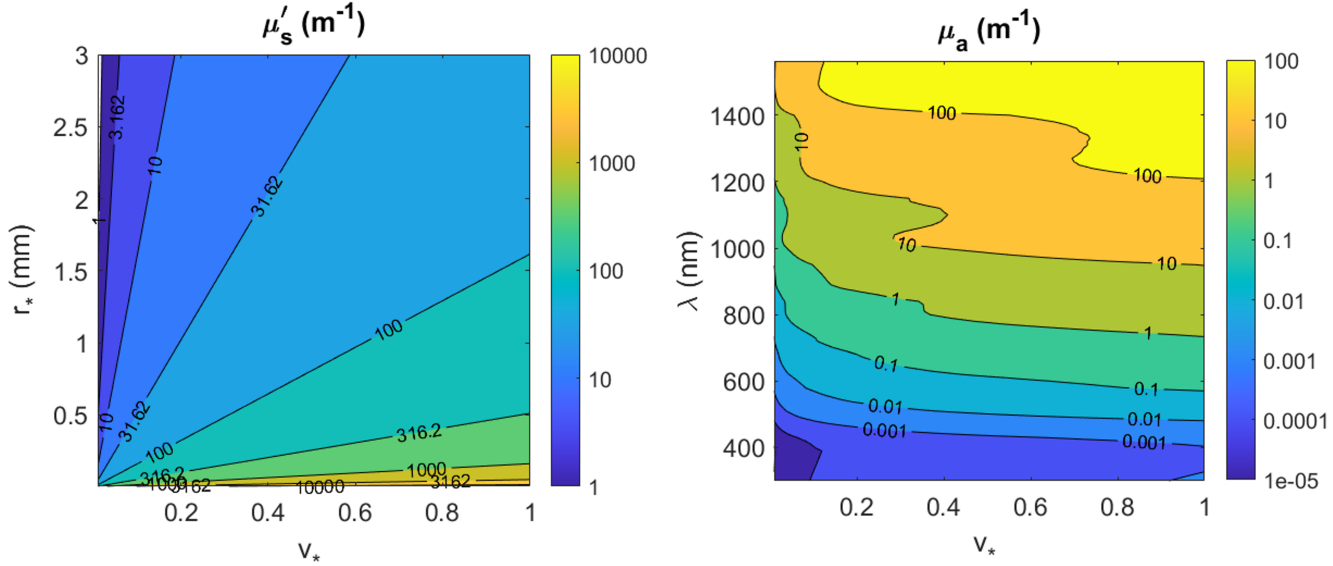


Fig. 2. (a) Effective scattering coefficient μ'_s (1/m) as a function of ice volume fraction v_* (unitless) and grain radius r_* (mm). Values computed for 640 nm light, such that $Q_s = 2.0053$ and $g = 0.8926$ (Sumlin and others, 2018). (b) Absorption coefficient μ_a (1/m) of clean snow as a function of ice volume fraction v_* (unitless) and wavelength λ (nm).

scattering asymmetry factor g as a function of grain radius, wavelength, and the complex refractive index at the chosen wavelength (Warren and Brandt, 2008). The absorption and effective scattering coefficients of the snowpack are then computed as follows:

$$\mu_a = Q_a \pi r_*^2 N_* = \frac{3Q_a v_*}{4r_*} \quad (5)$$

$$\mu'_s = Q_s(1-g) \pi r_*^2 N_* = \frac{3Q_s(1-g)v_*}{4r_*}, \quad (6)$$

where N_* is the number density of ice grains in the snowpack. In theory, the values of Q_a , Q_s , and g display a highly non-linear and oscillatory dependence on the grain size r_* . This oscillatory “ringing” is an artifact of the assumption that all grains have precisely the same radius—a condition that is never satisfied by real snow. When the oscillations are smoothed out, Q_s , g , and the ratio Q_a/r_* become nearly independent of grain size at visible and near-infrared wavelengths, so long as the grains are not unreasonably large. We thus treat these values as wavelength-dependent constants, computed by taking their average value across a range of feasible grain sizes at the wavelength of interest. Doing so dramatically simplifies our model— μ_a becomes independent of grain size and depends linearly on v_* , and μ'_s depends only on the ratio v_*/r_* .

In Fig. 2(a) we visualize the range of values for μ'_s obtained across a domain of feasible grain sizes and ice volume fractions. The values shown here were computed for a wavelength of 640 nm—however, because Q_s and g are only weakly dependent on wavelength, the μ'_s values shown in Fig. 2(a) are comparable to those that would be obtained across a large fraction of the visible and near-infrared spectrum. Figure 2(b) shows the dependence of μ_a , obtained using Eq. 5, on ice volume fraction and wavelength. Unlike μ'_s , the

absorption coefficient depends strongly on wavelength, and varies by more than an order of magnitude between the red ($\lambda = 640$ nm) and near infrared ($\lambda = 905$ nm) wavelengths used in this study.

The last parameter that we must calculate is the speed of light within the snowpack c_* . In many problems that involve light propagation in a scattering medium, light's speed is treated as a constant that can be computed beforehand if the medium's index of refraction is known. This approach does not work for snow, which is a heterogenous mixture of two materials—ice and air—that have markedly different refractive indices and that may be mixed at any ratio.

We follow the lead of Smith and others (2018) and use the *mean* speed of light within the snowpack, which can be derived from the expected fraction of a photon's path that passes through ice, and through air. This value is necessarily dependent upon the ice volume fraction, and can be written as

$$c_* = \frac{c_0}{1 + (n_{ice} - 1)v_*}, \quad (7)$$

where n_{ice} is the real component of the index of refraction of ice and c_0 is the speed of light in air (where it's assumed that $n = 1$).

Having obtained expressions that relate μ_a , μ'_s , and c_* to the grain size and ice volume fraction of a clean snowpack, we can now develop an understanding of how changes to v_* and r_* affect the snowpack's time-domain optical response. Upon inspection of Eq. 4, we see that the shape of a snowpack's transient response is primarily controlled by $\mu_a c_*$, which determines the rate of decay of the signal's tail; $2Dc_*$, which can be interpreted as the rate at which a Gaussian cloud of diffusing photons expands over time, and which controls the position of the signal's peak; and z_0^2 , which influences the shape of the response at the earliest arrival times, but in practice has little effect when $s \gg z_0$.

The exponential decay rate, $\mu_a c_*$, only depends on v_* . On the other hand, $2Dc_*$ and z_0^2 primarily depend on the medium's scattering coefficient, which in turn depends on the ratio v_*/r_* . These effects are visualized in Figs 3(a) and (b), where we plot the predicted transient response curves for snowpack with varying v_* and r_* . For these curves, the snow is probed with red (640 nm) light, and the position of the detector's focus spot is fixed at $s = 8$ cm.

In Fig. 3(a), we see that as v_* is increased while r_* is held constant, the slope of the signals' exponential tail becomes more steep as light is absorbed by the medium more quickly. The arrival time of the signal peak is also pushed back because tighter packing of the ice grains reduces the distance between photon scattering events, thus reducing the rate at which light diffuses within the medium. In Fig. 3(b), r_* is varied while v_* is held constant. As grain size increases, grains must be spaced further apart to maintain the same density, thus increasing the rate of diffusion within the medium. As such, for a fixed snow density and source-detector separation, the peak of the diffusion signal will arrive earlier, and will be more intense, when the grains are large.

In Fig. 3(d), v_* and r_* are held fixed and the detector focus position s is varied. As s increases, the signal peak arrives later and becomes more faint. However, as time passes, all signals converge as light spreads within the medium and the distribution of emitted photons becomes nearly uniform across the observed region.

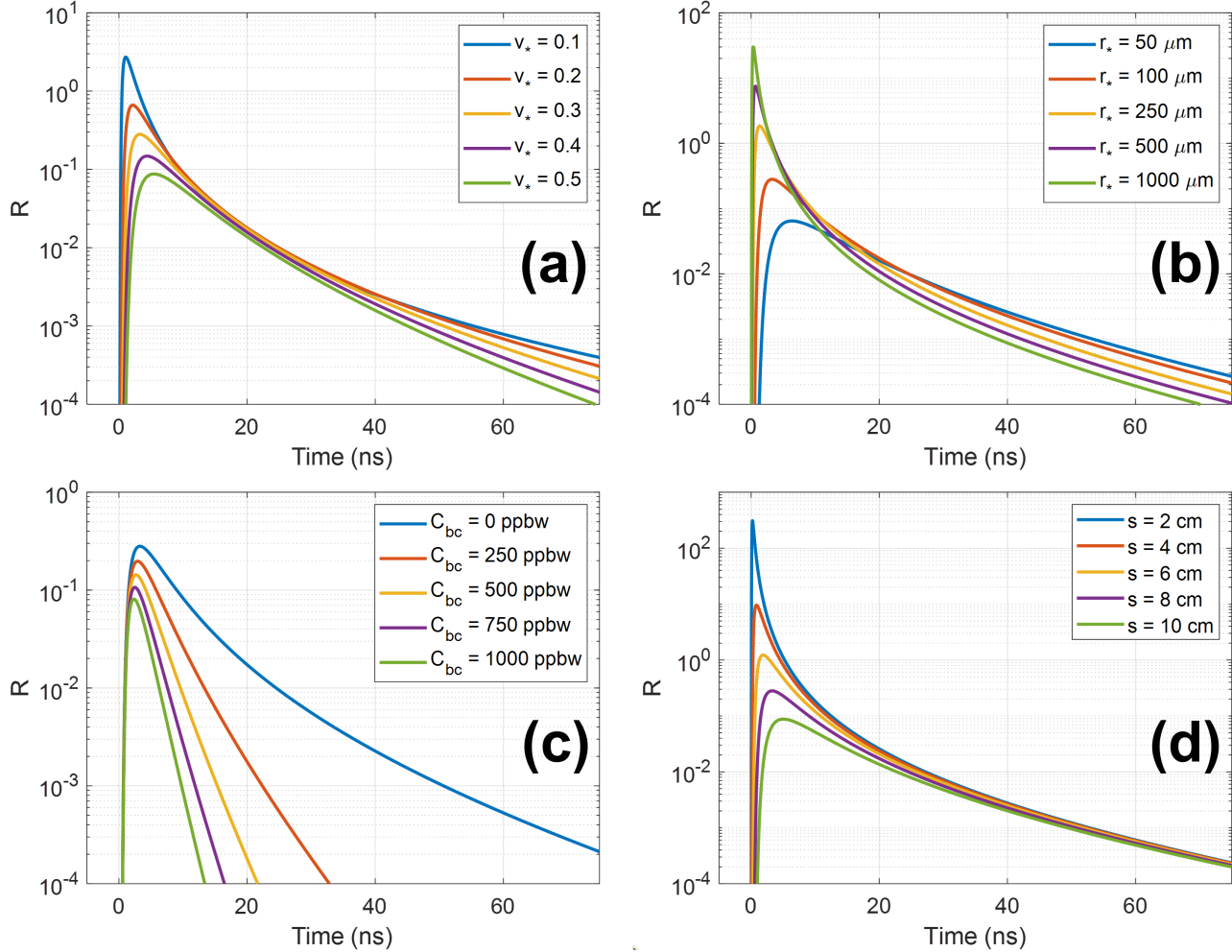


Fig. 3. Plots of predicted time-dependent flux measured by a detector observing snow following illumination by a laser pulse ($\lambda = 640$ nm). Curves were produced using Eq. 4 and μ_a , μ'_s , and c_* were computed from v_* , r_* , and C_{bc} using Eqs. 9, 6, and 7, respectively. (a) Ice volume fraction v_* is varied. r_* = 100 μm , C_{bc} = 0 ppbw, and s = 8 cm. (b) Grain radius r_* is varied. v_* = 0.3, C_{bc} = 0 ppbw, and s = 8 cm. (c) Impurity concentration C_{bc} is varied. v_* = 0.3, r_* = 100 μm , and s = 8 cm. (d) Detector focus position s is varied. v_* = 0.3, r_* = 100 μm , and C_{bc} = 0 ppbw.

The Effect of Light Absorbing Impurities

Ice is an exceptionally weak absorber of light, particularly at visible wavelengths (Warren, 2019). As such, the absorption of light within a snowpack can be enhanced significantly—even dominated—by the presence of trace concentrations of more absorptive substances. This has the important effect of reducing snowpack albedo, which increases radiative forcing on the snow surface and subsequently enhances snow melt and metamorphism and can also influence the local climate (Skiles and others, 2018). For our purposes, the presence of small concentrations of LAPs can increase the absorption coefficient of a snowpack considerably—thus rendering Eq. 5, our model for clean snowpack absorption, insufficient. Globally, radiative forcing from LAPs is dominated by black carbon, mineral dust, organic or “brown” carbon, and snow algae (Skiles and others, 2018). Here we assume that absorption by LAPs is dominated by black carbon, but note that our model could be extended to include other types of particles by modifying the LAP absorption spectrum used here.

The presence of black carbon in a snowpack alters its properties primarily by adding an extra term to the absorption coefficient, i.e. $\mu_a^{snow} = \mu_a^{ice} + \mu_a^{bc}$. This additional term can be computed from the dispersed (rather than bulk) density ρ_{bc} and the wavelength-dependent mass absorption efficiency MAE_{bc} (m^2/kg) of the black carbon particles (Grenfell and others, 2011), as follows:

$$\mu_a^{bc} = MAE_{bc}\rho_{bc} = MAE_{bc}\rho_{ice}C_{bc}v_*. \quad (8)$$

On the right side of Eq 8, we replace ρ_{bc} with the product of the bulk density of ice ($\rho_{ice} = 916.5 \text{ kg/m}^3$), the mass mixing ratio of black carbon in the snow C_{bc} , and the snowpack’s ice volume fraction v_* . We then combine Eqs. 5 and 8 to obtain a complete expression for the snowpack absorption coefficient:

$$\mu_a = \left(\frac{3Q_a}{4r_*} + MAE_{bc}\rho_{ice}C_{bc} \right) v_*. \quad (9)$$

Following the example of Doherty and others (2014), we model the wavelength dependence of MAE_{bc} using a power law spectrum:

$$MAE_{bc}(\lambda) = MAE_{bc}(\lambda_{ref}) (\lambda_{ref}/\lambda)^{\text{Å}}, \quad (10)$$

that has an Ångstrom coefficient $\text{Å} = 1.1$ and is referenced to $MAE_{bc}(\lambda_{ref}) = 6500 \text{ m}^2/\text{kg}$, where $\lambda_{ref} = 600 \text{ nm}$.

Fig. 4 illustrates that, for a fixed C_{bc} , the fraction of absorption attributable to black carbon in snow depends strongly on the wavelength of light that interacts with the snowpack. We plot the ratio of absorption due to black carbon (using Eq. 8) to the total absorption (from Eq. 9) for a selection of wavelengths that ranges from 400 nm (blue) to 1000 nm (near infrared). For blue light, our model suggests that absorption is entirely dominated by just 1 ng/g of black carbon, which is comparable to mass mixing ratios found in Greenlandic snow (Warren, 2019). In contrast, at 1000 nm, absorption from black carbon only eclipses ice absorption for mass mixing ratios above 7500 ng/g—a very high level of soot that would cause the snow to appear visibly grey. This decreased sensitivity at longer wavelengths is not caused by the decreased absorption of black carbon at these wavelengths, but rather by the increased absorption

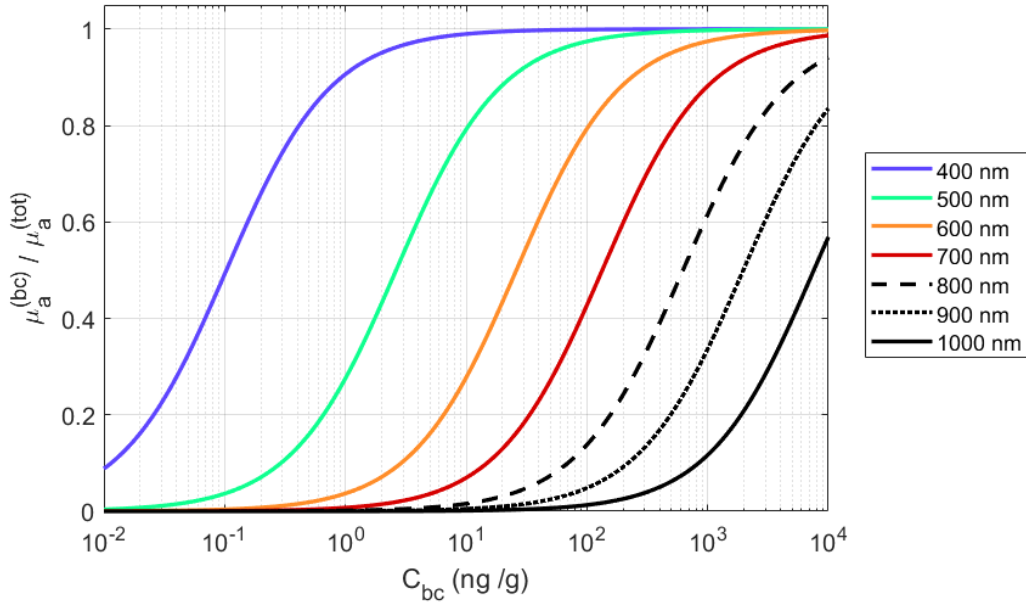


Fig. 4. The ratio of light absorption due to black carbon (Eq. 8) to total absorption by the snowpack (Eq. 9) for a range of wavelengths.

efficiency of ice.

In Fig. 3(c), we show how changes to C_{bc} affect that snowpack's time-domain optical response. We plot transient response curves for snow samples with a variety of black carbon concentrations. These curves assume a laser wavelength of 640 nm and a fixed grain radius, ice volume fraction, and focus spot position. Black carbon content only influences the absorption coefficient of the snowpack, and the effect of this is to steepen the exponential decay rate $\mu_a c_*$. At the probing wavelength of 640 nm this effect is quite dramatic when compared to the comparable influence of ice volume fraction on the exponential decay rate, which is shown in in Fig. 3(a).

Non-spherical Grains

Although the assumption of spherical ice grains has been used successfully for many applications (Wiscombe and Warren, 1980a; Nolin and Dozier, 2000), it is not strictly correct as real snow often contains strikingly non-spherical grain shapes (Bentley and Humphreys, 1931). Scattering models for non-spherical ice grains have been developed (Kokhanovsky and Zege, 2004; Flanner and others, 2021). Non-spherical grain models introduce two additional degrees of freedom, the scattering asymmetry factor g and an “absorption enhancement parameter” B that accounts for internal reflections within the ice grains (Kokhanovsky and Zege, 2004).

We elected to use a spherical grain model because we assumed that these additional degrees of freedom would prevent direct retrieval of v_* , r_* , or C_{bc} . Recently, (Robledano and others, 2023) argued that while g and B vary significantly among idealized grain shapes such as spheres, cubes and fractals, g and B for natural snow samples do not vary very much, and cluster around the predicted values for a random two-phase medium. Such findings suggest that it should be possible to both accurately account for grain

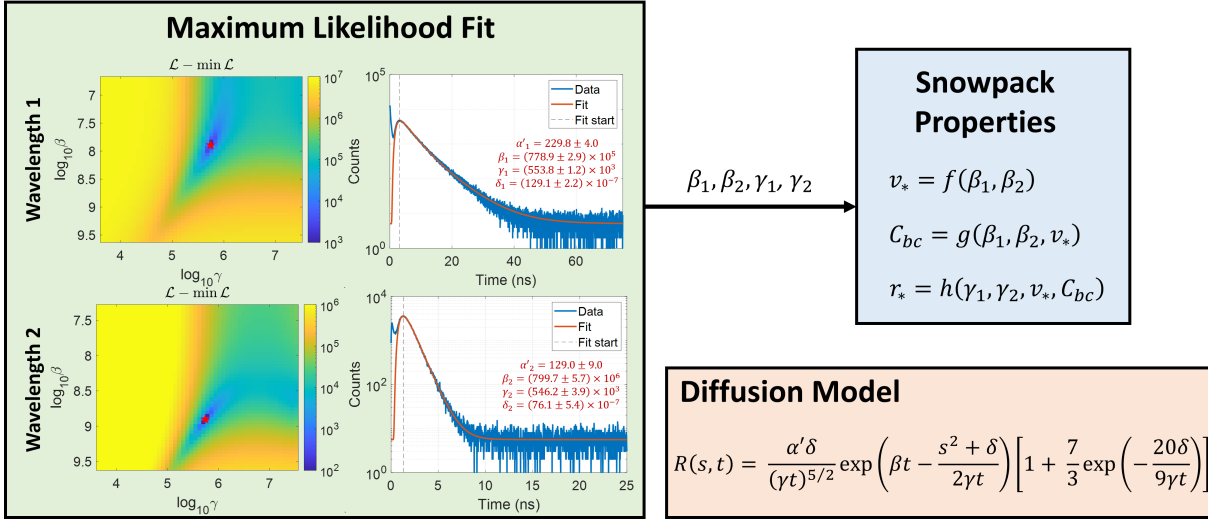


Fig. 5. (Left) A diffusion model (lower right) is fit to photon time-of-flight histograms measured at two wavelengths. Fit parameters α' , β , γ , and δ are determined using a grid search algorithm that minimizes a negative Poisson log-likelihood function. (Top right) Snowpack properties v_* , r_* , and C_{bc} are computed directly from parameters β_1 , β_2 , γ_1 , and γ_2 by evaluating analytical expressions (Eqs. 15, 16, and 17)

asphericity and unambiguously retrieve v_* , r_* , or C_{bc} . In future work, we will apply the findings of (Robledano and others, 2023) to our inversions and determine the effect of asphericity on the results.

Algorithm

We fit functions of the same form as Eq. 4 to two photon time-of-flight histograms—each measured using a different laser wavelength. We use a grid search to find the fit parameters that minimize a negative Poisson log-likelihood function that properly accounts for photon count statistics. The parameters of the fitted curves are then used to compute the snowpack properties v_* , r_* , and C_{bc} . A visualization of our retrieval algorithm is shown in Fig. 5.

Fit Parameterization

We re-parameterize Eq. 4 in terms of the fitting parameters $\alpha' = \frac{\alpha c_*}{3(2\pi)^{3/2}}$, $\beta = \mu_a c_*$, $\gamma = 2D c_*$, and $\delta = z_0^2$. This allows for the model to be expressed in simplified form:

$$R(s, t) = \alpha' \frac{\delta}{(\gamma t)^{5/2}} \exp\left(-\beta t - \frac{s^2 + \delta}{2\gamma t}\right) \left[1 + \frac{7}{3} \exp\left(-\frac{20\delta}{9\gamma t}\right)\right]. \quad (11)$$

Although Eq. 11 appears to have four degrees of freedom, only the exponential decay rate parameter β and the spatial spread rate γ are used to estimate snowpack properties in practice. Interpreting the scaling constant α' requires precise calibration of the instrument and measurement geometry which is challenging in practice and which we did not attempt. Eq. 11 also depends only weakly on the squared source depth δ , to the point that accurate estimates of δ are almost never obtained.

The spatial spread rate γ depends primarily on μ'_s and c_* , which are largely independent of the measurement wavelength for visible and near-infrared light. Altogether, this means that $n + 1$ independent

parameters can be retrieved from measurements taken at n wavelengths. If absorption due to light absorbing particles is known to be insignificant (i.e. $\mu_a^{bc} \ll \mu_a^{ice}$), then v_* and r_* can be retrieved from measurements at a single wavelength. Otherwise, retrieving v_* , r_* , and C_{bc} requires measurements at least two wavelengths.

Maximum Likelihood Estimate of Model Parameters

The number of counts in a histogram timing bin centered at t_i is assumed to be a Poisson random variable with a rate parameter x_i , defined as

$$x_i = R(s, t_i; \Theta) + b = \alpha' r_i + b, \quad (12)$$

where R is the flux predicted by Eq. 11 at position s , time t_i , and for parameters $\Theta = \{\alpha', \beta, \gamma, \delta\}$. The rate of background counts produced by ambient light, detector dark counts, and detector afterpulsing (Zappa and others, 2007) is denoted by b , and is assumed to be constant with respect to time. The variable r_i denotes the normalized predicted flux, for which $\alpha' = 1$.

The probability of observing a vector of time-binned measurements \mathbf{y} given a vector of predicted count rates \mathbf{x} is

$$P(\mathbf{y}|\mathbf{x}) = \prod_{\Delta}^N \frac{x_i^{y_i} e^{-x_i}}{y_i!} \quad (13)$$

where N denotes the total number of timing bins in the histogram and Δ is the starting bin for the curve fit. We seek to find the parameters α' , β , γ , δ , and b that minimize the negative Poisson likelihood:

$$\mathcal{L}(\mathbf{x}, \Theta, b|\mathbf{y}) = -\ln P(\mathbf{y}|\mathbf{x}) = \sum_{\Delta}^N x_i - y_i \ln x_i + \ln y_i!. \quad (14)$$

We find the set of parameters that minimizes the negative log likelihood using a grid search. To reduce the dimensionality of the search, we first estimate b by computing the mean number of counts in a designated set of noise bins that reliably contains effectively zero non-background counts. For any combination of β , γ , and δ , the scaling term α' can then be estimated using the expression $\bar{\alpha}' = \sum_{\Delta}^N (y_i - b) / \sum_{\Delta}^N r_i$.

We can thus define a three-dimensional search area that contains all feasible values of β , γ , and δ . The feasible range for δ is tightly constrained to $\left(\frac{3\gamma}{2c_0}\right)^2 < \delta < \left(\frac{3n_{ice}\gamma}{2c_0}\right)^2$, which allows for a coarse fit to be obtained using an effectively two-dimensional search.

We perform a sequence of nested searches—we first obtain a coarse fit, then define a small search range around the fitted parameters and repeat the search using a smaller grid cell size. This procedure is iterated until a fit with the desired precision is obtained. Our fitting algorithm was implemented in MATLAB on a Lenovo Thinkpad T590 laptop with 16GB of RAM. Run time per fit was typically 56 seconds for 640 nm histograms, and 19 seconds for 905 nm histograms (which had fewer timing bins). Curve fits obtained using our algorithm are shown in Fig. 5. We estimated the uncertainty in the retrieved values of β , γ , and δ by computing the inverse of the Hessian of the loss function at the estimated minimum, and then taking the diagonal terms.

Computing v_* , r_* , and C_{bc}

When measurements are obtained at two wavelengths, λ_1 and λ_2 , the ice volume fraction v_* and black carbon mixing ratio C_{bc} can be extracted from the decay parameters β_1 and β_2 . Each term β_i can be expressed as a function of v_* and C_{bc} by taking the product of Eqs. 7 and 9. This results in a set of two equations which can be solved, first, for v_* :

$$v_* = \frac{b_2\beta_1 - b_1\beta_2}{c_0(a_1b_2 - a_2b_1) - d_1b_2\beta_1 + d_2b_1\beta_2}. \quad (15)$$

For notational simplicity we have made the substitutions $a_i = \frac{3}{4} \left[\frac{Q_a}{r_*} \right]_i$, $b_i = \rho_{ice}MAE_{bc}(\lambda_i)$, and $d_i = n_{ice}(\lambda_i) - 1$. As was justified previously, we treat the ratio $\left[\frac{Q_a}{r_*} \right]$ as a constant with respect to r_* that depends only on wavelength. As before, the term c_0 refers to the speed of light in air.

Once v_* has been obtained, C_{bc} can be computed as follows:

$$C_{bc} = \frac{1}{c_0b_1} \left[\left(\frac{1}{v_*} + d_1 \right) \beta_1 - c_0a_1 \right] = \frac{1}{c_0b_2} \left[\left(\frac{1}{v_*} + d_2 \right) \beta_2 - c_0a_2 \right]. \quad (16)$$

After v_* and C_{bc} have been computed, the grain radius r_* can be computed from the spatial spread parameter γ_i at either wavelength:

$$r_* = e_i \left[\frac{2c_0}{3\gamma_i v_*(1 + d_i v_*)} - a_i - b_i C_{bc} \right]^{-1}. \quad (17)$$

Here a_i , b_i , and d_i are defined as they were previously, and $e_i = 3Q_{s,i}(1 - g_i)/4$. Because r_* can be computed using either γ_1 or γ_2 , we evaluate Eq. 17 at both wavelengths, and then take the uncertainty-weighted average of the two values obtained in this way to arrive at our final estimate for r_* . Uncertainties in v_* , r_* , and C_{bc} are obtained via error propagation from uncertainties in β_1 , β_2 , γ_1 , and γ_2 .

If it is known that absorption by light absorbing particles is small compared to absorption by ice grains, then v_* and r_* can be computed from the fit parameters extracted from single-wavelength measurements. First v_* can be computed from the exponential decay rate β , as follows:

$$v_* = \frac{\beta}{ac_0 - \beta d}, \quad (18)$$

and then r_* can be obtained from the spatial spread rate γ , and our estimate of v_* :

$$r_* = e \left[\frac{2c_0}{3\gamma v_*(1 + dv_*)} - a \right]^{-1}. \quad (19)$$

Here a , b , d , and e retain their meanings from Eqs. 15 and 17.

Evaluation Using Simulated Measurements

We validated our algorithm using a GPU-accelerated Monte-carlo photon transport simulation (Henley, 2020), which was adapted from a simulator originally developed for tissue imaging studies (Satat, 2019). We modeled the propagation of photons within a semi-infinite, homogeneous scattering medium. The

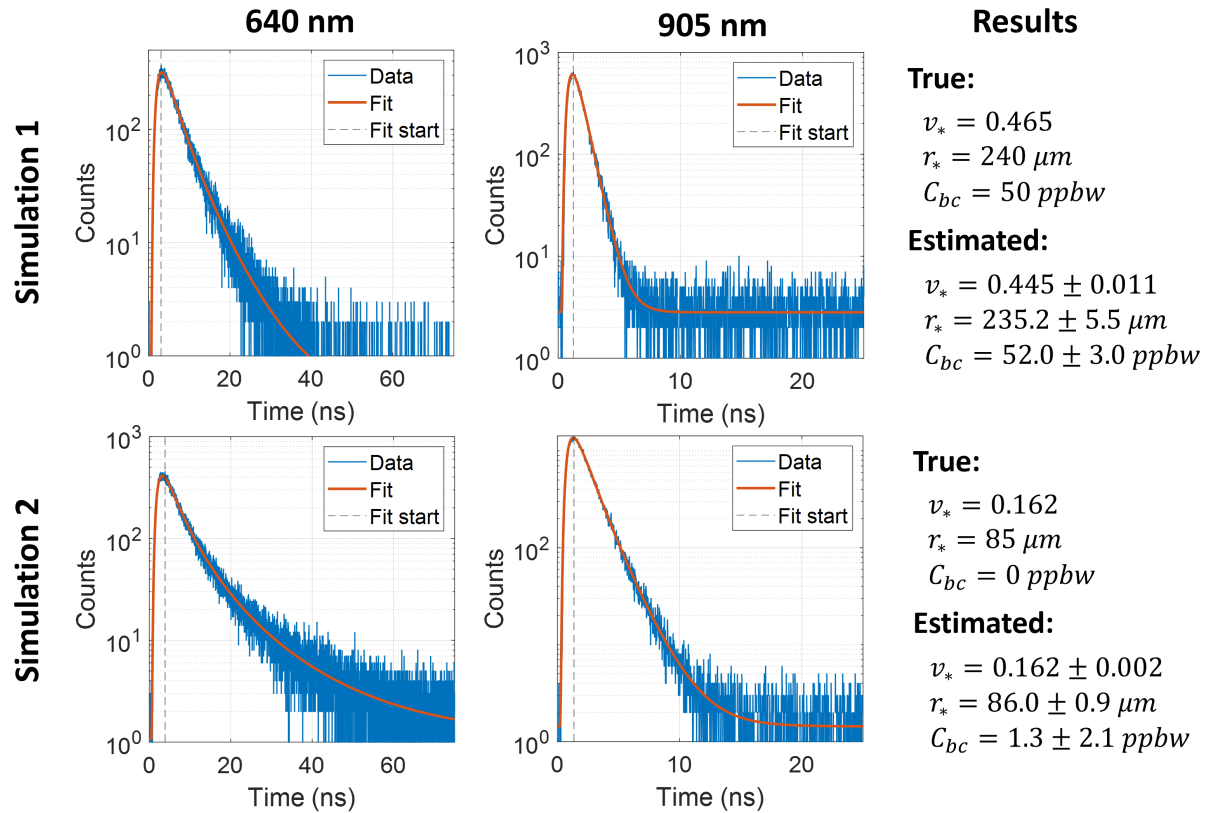


Fig. 6. We used a monte-carlo photon transport simulator to validate our retrieval algorithm. Measurements were simulated for 640 nm (left) and 905 nm (center) light for two simulated snow samples. True and estimated snowpack parameters for each sample are shown on the right.

medium's properties μ_a , μ'_s , and c_* were computed from v_* , r_* , and C_{bc} using Eqs. 6, 7, and 9. To simulate pencil-beam illumination, photons were launched at the origin ($[x, y, z] = \mathbf{0}$) at time $t = 0$ and at normal incidence to the snow surface. Photons scattered randomly in the medium until they were absorbed, exited the medium, or satisfied an outlier termination criterion such as maximum number of scattering events. For more details, we refer the reader to Chapter 4 of (Welch and van Gemert, 1995).

We simulated photon time-of-flight histograms at 640 nm and 905 nm measurement wavelengths for two snow samples with different properties. We binned photons by the transverse position s (bin width 1 cm) and time t (bin width 16 ps) that photons exited the snow surface. For 640 nm measurements, photons detected at $s = 10.0 \pm 0.5$ cm were used for curve fitting, whereas for 905 nm measurements photons detected at $s = 7.0 \pm 0.5$ cm were used. Once a histogram of signal photons was created, a random number of background counts was added to each timing bin by sampling from a Poisson distribution with rate parameter b that was chosen to be consistent with the uniform background count levels observed in experimental measurements.

Our results are shown in Fig. 6. For the first simulation, the true snowpack properties were $v_* = 0.465$, $r_* = 240 \mu\text{m}$, and $C_{bc} = 50 \text{ ppbw}$. Our method retrieved values of $v_* = 0.445 \pm 0.011$, $r_* = 235.2 \pm 5.5 \mu\text{m}$, and $C_{bc} = 52.0 \pm 3.0 \text{ ppbw}$. For the second simulation, the true snowpack properties were $v_* = 0.162$, $r_* = 85 \mu\text{m}$, and $C_{bc} = 0 \text{ ppbw}$. Our method retrieved values of $v_* = 0.162 \pm 0.002$, $r_* = 86.0 \pm 0.9 \mu\text{m}$, and $C_{bc} = 1.3 \pm 2.1 \text{ ppbw}$. These results suggest that our algorithm should produce accurate estimates of snow properties if our snow scattering model is correct.

MATERIALS

Apparatus

Lidar System

We assembled a simple lidar system to measure the time-domain optical response of a variety of snow samples. Photographs of our experimental setup are shown on the left in Fig 7. Our lidar system used a single-pixel SPAD detector (Microphoton Devices PDM series) with a timing jitter of ~ 50 ps (FWHM), and two pulsed diode laser sources—a red laser with a wavelength of 640 nm (Picoquant LDH-P-C-640B), and a near-infrared laser with a wavelength of 905 nm (Picoquant LDH-P-C-905). Each laser was operated at a pulse repetition frequency of 2.5 MHz and had a quoted pulsedwidth of < 90 ps. The 640 nm laser was operated at a time-averaged power of $80 \mu\text{W}$, and the 905 nm laser was operated at a time-averaged power of $55 \mu\text{W}$. A Picoquant Hydralarp 400 was used to synchronize the arrival times of detected photons with the laser repetition rate. The overall instrument response function (IRF) of the system was measured to be 128 and 160 ps (FWHM) for 640 and 905 nm measurements, respectively.

Measurement Procedure

Experiments were conducted in a cold room at -1°C . A large folding mirror was used to direct the lidar beam and detector field of view (FOV) towards a cooler filled with snow that was placed on the floor. Because only a single laser diode could be operated at any one time, 640 nm measurements were collected

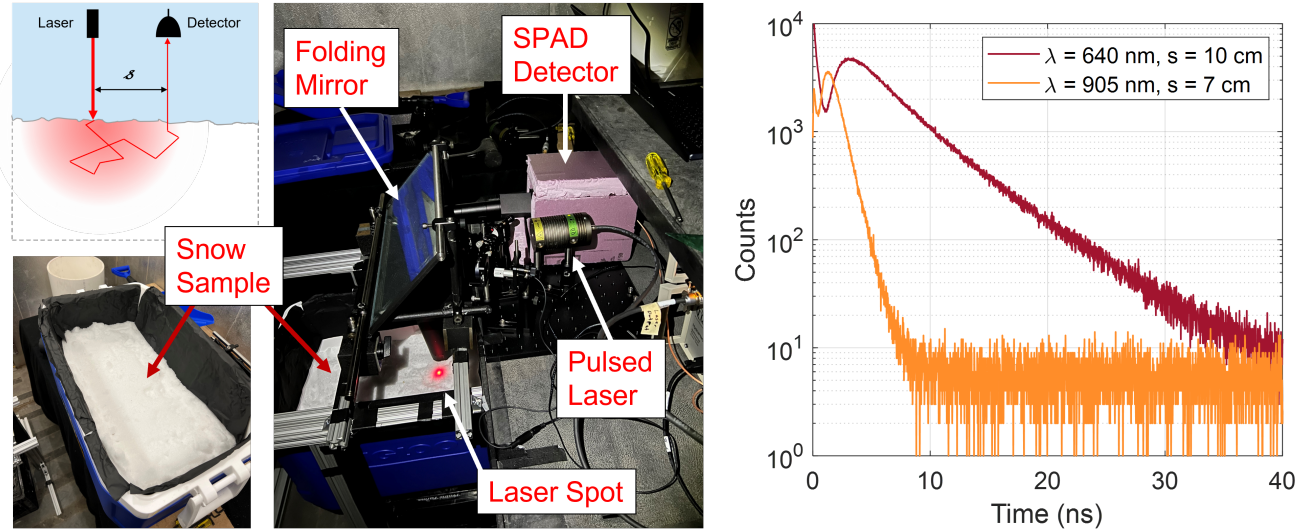


Fig. 7. (Left) Photos depicting our experimental setup. Snow was held in a cooler placed on the floor, and illuminated using pulsed diode lasers at two wavelengths (640 nm, 905 nm). A single-photon avalanche diode measured the time-of-flight of photons that exited the snow surface at distance s from the laser spot. (Right) Time-of-flight histograms measured using our system. For this test the snow sample consisted of natural snow that had been aged for nine months at -10°C .

first. During these measurements, a red bandpass filter (Edmund Optics TECHSPEC 650nm/50nm) was placed in front of the detector to suppress interference from ambient background light. Following these measurements the 640 nm laser head and bandpass filter were removed and replaced with the 905 nm laser head and a near-infrared bandpass filter (Thorlabs FL905-10). We then collected a second set of measurements.

The beam from either laser head could be scanned by hand using a steering mirror. A lens was placed in front of the detector to focus its FOV to a small spot ($< 1 \text{ cm FWHM}$) on the snow surface. To find this focus spot, the laser beam would be steered to the point on the surface at which detector counts were maximized. Once the focus spot was found, a laser pointer (distinct from the pulsed diode lasers) was steered to mark the position of the focus spot. The *pulsed* beam could then be steered to a point on the snow surface that was displaced from the focus spot by a small distance s that was measured using a ruler. The focus-marker beam would then be switched off. When the 905 nm laser was in use, a phosphorescent laser viewing card was used to find the position of the laser spot on the snow surface.

We note that even when the laser and focus spots were separated by several centimeters, interference from direct returns off of the snow surface remained significant due to phenomena such as lens flare. Although we could not suppress this interference entirely, we were able to mitigate it by placing a long lens tube in front of our detector that functioned as a baffle.

For each snow sample, and for each laser wavelength, we collected measurements at multiple source-detector separations s . Each measurement consisted of a histogram of photon arrival times with 16 ps timing bins that spanned a 250 ns timing window. Examples of histograms measured by our lidar system are shown on the right in Fig. 7. The first measurement would always be collected at $s = 0 \text{ cm}$ to measure the time-of-arrival of photons that scattered directly off of the snow surface. The peak of this direct

return would serve as a reference time for all subsequent measurements. Direct surface returns were always measured with a 60 second integration time, with a neutral density filter placed in front of the detector to prevent saturation, and with a wooden ruler placed on the snow surface at the position of the laser spot to prevent bias due to subsurface scattering. Following this, histograms would be collected for one or more non-zero source-detector separations. We used an integration time of 10 minutes for each histogram collected with 640 nm light, and 30 minutes for each histogram collected with 905 nm light. A longer integration time was required at 905 nm because our SPAD detector was less sensitive at this wavelength, the output power of our laser was lower, and the snow itself was less reflective.

Before proceeding, we want to stress that our lidar system was assembled strictly for the proof-of-principle demonstrations documented in this paper. It was not optimized for ease of use or light collection efficiency. Although the integration times reported here are quite long, we expect that a cleverly engineered system might collect equivalent data with integration times that are far shorter—perhaps by several orders of magnitude. Integration time could be reduced significantly, for instance, by using a multipixel Silicon Photomultiplier (SiPM) in place of the single-pixel SPAD used here, and by using lasers with higher power and higher repetition rates. The use of laser sources and SPADs designed for a consumer electronics environment (King and others, 2023), rather than the optical bench equipment used here, would also allow for a system that was portable, rugged, and affordable. Altogether, this suggests that the development of a field-deployable system is a feasible goal—one which we hope to pursue in future work.

Samples

We performed two sets of experiments. In the first, samples had relatively low LAP concentrations but grain size and density varied significantly. In the second, the samples had varying amounts of black carbon mixed into them, but density and grain size was relatively constant.

All snow used in our experiment originated as natural snow harvested on Dartmouth College campus and was subsequently modified in various ways. When not being used for experiments, snow samples were stored in lidded coolers in a -10°C cold room.

Clean Snow Samples

We performed five sets of measurements on samples with varying density and grain size but relatively low LAP content. The snow used in the first set of measurements was harvested after a snowfall in March 2022 and then kept in a -10°C cold room for nine months. By the time measurements were taken, the snow had become more dense and the grains had metamorphosed into medium size rounded grains and rounding faceted particles (Fierz and others, 2009). The next three data collections were performed on a single snow sample that was modified between measurements. Measurements were first collected immediately after the snow had fallen, when the snow had a very low density and consisted of precipitation particles (Fierz and others, 2009), with many stellar dendrites. A second set of measurements was collected after the snow had been compacted with a shovel—thus increasing its density but leaving grain size and shape relatively unchanged. The third set of measurements was collected after the snow was aged for three weeks at -10°C and then for one day at 0°C . This aging produced a clear change in grain shape, to small rounded

grains and decomposing precipitation particles, and a small increase in grain size and density. For our final set of measurements we harvested snow that had been sitting outside for weeks, where it had experienced several melt and re-freeze events. This snow had very high density and coarse grains.

At the time of data collection, all samples were held in coolers with approximate internal dimensions of 50 cm×25 cm×30 cm and that had matte white internal walls. Snow would fill the cooler to varying degrees, but was typically at least 20 cm deep, relative to the cooler bottom.

Soot Addition Experiments

For the second set of experiments, we filled five Styrofoam coolers (dimensions 17.5 cm×23.5 cm×24.0 cm) with freshly fallen snow. We then mixed small amounts of Sigma-Aldrich Fullerene Soot into the samples, such that the five respective samples had 0, 1, 2, 3, and 4 baseline units of soot. To add soot to the snow in a controlled fashion, we created a soot-water suspension with a known concentration of soot, and then applied controlled volumes of the suspension to each snow sample with a spray bottle. The soot was mixed evenly into the snow using an ice scraper.

After performing a first set of measurements on the sooty samples we found that the added soot had a weaker effect on the snowpack absorption coefficients than had been expected. Following this finding, we approximately doubled the added soot concentration in all samples and repeated the measurements.

Ground Truth Measurements

Ground truth ice volume fraction was measured by extracting a small core (depth ~5 cm) from the snow surface. We measured the volume of snow in the core. The snow was then allowed to melt, and we measured the volume of the meltwater. Ice volume fraction was computed from the snow and meltwater volumes using conservation of mass.

Ground truth grain size was measured by imaging a small, snow-filled test tube (1.4 cm internal diameter) with a SkyScan 1172 microCT scanner (40 kV, 250 μ A source, 17 μ m resolution). Bruker NRecon software was used to reconstruct a 3D image of the sample. Following guidance from Hagenmuller and others (2016), the image was then blurred with a Gaussian kernel (radius 1 pixel), binarized with Otsu's method, and morphologically "opened" (radius 1 pixel). The surface area to volume ratio (SA/V) of the imaged sample was then computed two times using Bruker's CTAN software, following marching squares (2D analysis) and marching cubes (3D analysis) surface reconstructions. We computed the grain radius from each SA/V ratio independently, and then used the average of these two values as ground truth.

Ground truth estimates of black carbon concentration were obtained using a single particle soot photometer (SP2; Droplet Measurement Technologies), in a manner similar to that reported in Lazarcik and others (2017). Each snow sample was melted and ultrasonicated for at least 15 minutes prior to analysis. The liquid snow samples were aerosolized using an ultrasonic nebulizer (CETAC U5000AT), which removes moisture from the liquid stream before passing aerosols such as black carbon onto the SP2. The SP2 estimates black carbon particle mass via measurements of laser-induced incandescence. This system was calibrated using a series of fullerene soot standards. To avoid saturating the SP2, snow samples that were expected to have particularly high black carbon concentrations were diluted with MilliQ water by a

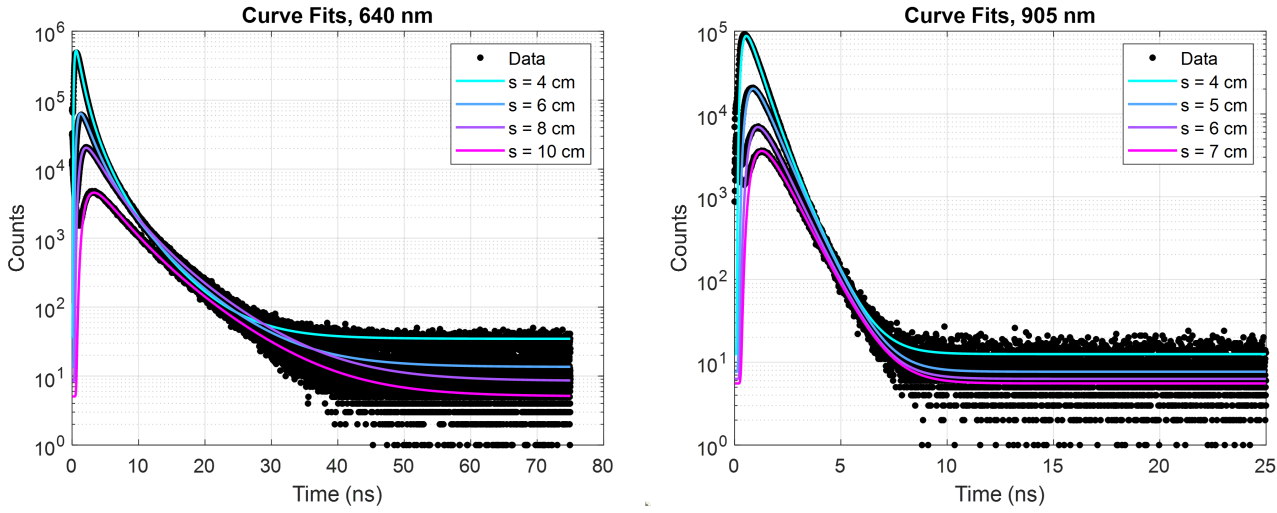


Fig. 8. Raw measurements collected for a single snow sample. Time-of-flight histograms were measured at two wavelengths (640 nm, 905 nm) and for four source-detector separations per wavelength. A diffusion model was fit to each histogram. The pair of curves with the best goodness of fit was used to compute snowpack properties.

factor of 6.

RESULTS

Clean Snow Experiments

Fresh Snow Sample

To provide insight into our data collection and fitting procedures, we first present a detailed review of all measurements collected for a single snow sample. This sample, which is described in greater detail in the Materials section, consisted of natural snow that had been aged for nine months in a $-10\text{ }^{\circ}\text{C}$ cold room.

The raw, time-of-flight histogram data collected for this sample, as well as our curve fits to those measurements, are shown in Fig. 8. Measurements were taken at four different source-detector separations for each wavelength: $s = 4, 6, 8$ and 10 cm at 640 nm , and $s = 4, 5, 6$ and 7 cm at 905 nm . As a rule of thumb, we would start each fit at a timing bin that corresponded to the peak of the diffusion signal. This was done to avoid fitting to the earliest arriving photons, which are poorly described by our diffusion model. Histograms were collected at multiple s values because it was not known *a priori* what range of s values would yield good diffusion curve fits. If s and μ'_s were both small, then photons in the signal peak would be poorly described by our diffusion model because they would exit the snowpack after too few scattering events. On the other hand, if s and μ'_s or μ_a were too large, the diffusion signal would be faint relative to background interference, and the fit would be poor.

In Fig. 9, we show how the retrieved snow properties varied with respect to our choices of source-detector separation at each wavelength. In general, estimates of v_* , r_* , and C_{bc} were relatively stable so long as good curve fits were obtained at both wavelengths, but diverged from the stable value when one or both of the curve fits were poor. As an example, it is evident in Fig. 9(c) that C_{bc} estimates are biased high at $s = 4\text{ cm}$, but are otherwise relatively insensitive to changes in s at either wavelength.

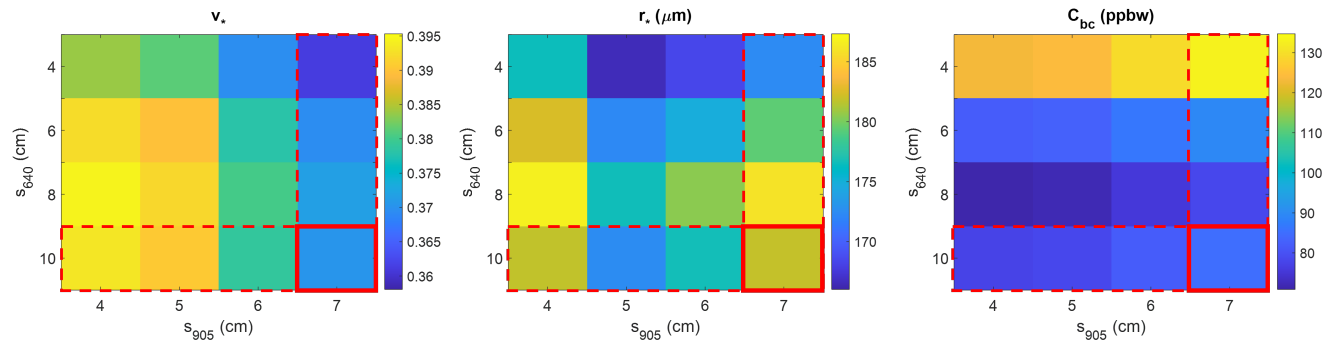


Fig. 9. Dependence of v_* , r_* , and C_{bc} estimates on choice of source-detector separation s for each measurement wavelength. Estimates that correspond to the pair of curve fits with the lowest reduced deviance (McCullagh, 2019) are outlined in red.

To arrive at a single estimate for v_* , r_* , and C_{bc} , we chose the curve fit at each wavelength with the lowest *reduced deviance* (McCullagh, 2019). Deviance is a goodness of fit metric that is appropriate for data that follows Poisson statistics, and that is asymptotically equivalent to χ^2 goodness of fit when the number of counts in all histogram bins is high. For the data collection described here, the best fits corresponded to $s = 10$ cm at 640 nm and $s=7$ cm at 905 nm. From the parameters of these two fits we estimated that $v_* = 0.370 \pm 0.003$, $r_* = 181.9 \pm 1.4$ μm , and $C_{bc} = 84.9 \pm 1.2$ ppbw. The ground truth measurements of these properties were 0.465, 242.5 μm , and 30.7 ppbw, respectively.

Full Results

We now present a summary of all results obtained for the clean snow samples described in the Materials section. The properties of the snow samples used in these tests varied widely, from light, fine-grained fresh powder to dense, coarse-grained snow that had experienced several melt and re-freeze events. In Fig. 10, we show a scatter plot of the densities and grain sizes estimated using our method, as well as ground truth values.

Our estimates of v_* , r_* , and C_{bc} are plotted with respect to ground truth in Fig. 11. In Fig. 11(a), we see a clear positive and nearly linear relationship between the ice volume fraction estimated using our technique, and ground truth, although estimates appear to be biased towards lower densities. The trends for r_* and C_{bc} are less clear, although our method appears to be capable of distinguishing between small and large grain sizes, and low and moderate impurity concentrations. To the extent that trends can be observed, r_* appears to be underestimated by a factor of ~ 2 , whereas C_{bc} appears to be over-estimated by a factor of ~ 2.5 .

In addition to dual-wavelength estimates of v_* , r_* , and C_{bc} , we also show estimates of v_* and r_* computed using only 905 nm measurements. Notably, the single-wavelength results match the dual-wavelength results very closely. Ice volume fraction estimates are slightly higher, which is consistent with excess absorption due to unmodeled LAPs. Single-wavelength grain size estimates are alternately higher or lower than corresponding dual-wavelength estimates.

Considering the very small statistical uncertainties in our results, we expect that the biases seen here are most likely attributable to model mismatch. In particular, the excess black carbon content predicted

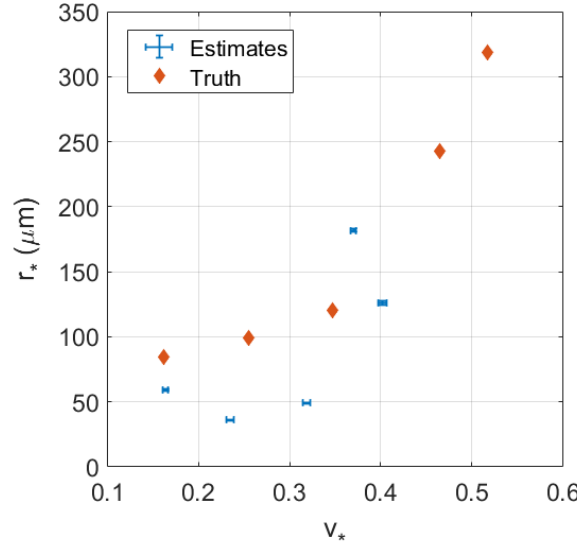


Fig. 10. Summary of the estimated and ground truth ice volume fractions v_* and grain sizes r_* of five clean snow samples. Error bars indicate one standard deviation.

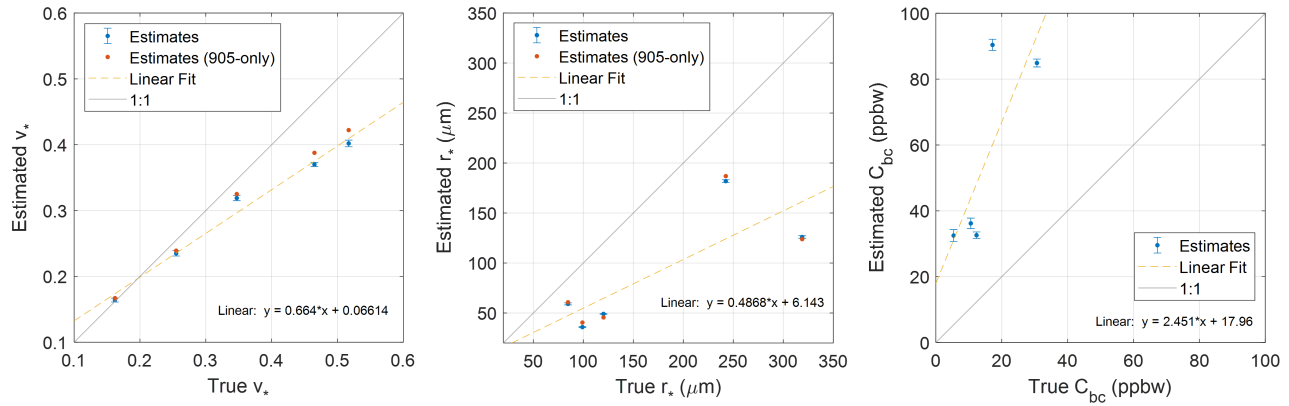


Fig. 11. Ground truth versus estimated values of ice volume fraction v_* , grain size r_* , and black carbon mass mixing ratio C_{bc} for five clean snow samples. Blue marks indicate estimates obtained using two measurement wavelengths (640 nm, 905 nm). Error bars indicate one standard deviation. Red marks indicate estimates of v_* and r_* obtained from 905 nm measurements only. Uncertainties were not computed for 905-only estimates.

by our method is plausibly explained by the presence of other kinds of light absorbing impurities such as dust. The samples used in this test were collected outdoors and were handled with shovels, ice scrapers, and various other equipment that may have been coated with dust or dirt. The smaller than expected grain size estimates are partly explained by the smaller than expected ice volume fraction estimates—in our method, v_* is estimated first and used as an input to Eq. 17 or Eq. 19 to compute r_* . Even accounting for this, grain size estimates are still lower than expected. The remaining bias is plausibly explained by the fact that our model assumes a scattering asymmetry factor g that is appropriate for spherical grains, but that is higher than the theoretical g value for the most common non-spherical grain shapes including spheroids, hexagonal plates, and fractals (Libois and others, 2013). By inspection of Eq. 6, we see that when g is assumed to be higher than the true value, predictions of r_* will be lower than the true value. Further investigation is needed to understand the biases in estimates of v_* . They are likely not explained by aspherical grain shapes, as the inclusion of a larger “absorption enhancement factor” that appropriately models common non-spherical grain shapes would have increased, not decreased, estimates of v_* . The effect of “close packing” of grains has been reported to reduce the absorption enhancement factor of snow (Libois and others, 2014). However, it is not clear that the snow samples used in this study were close-packed to an extraordinary degree.

Soot Addition Experiments

Here we present the results of the soot addition experiments described in the Materials section, where the snow samples contained varying concentrations of black carbon. For these tests, the source-detector separation was held fixed at $s = 8$ cm for 640 nm measurements. For 905 nm measurements, a value of $s = 5$ cm was typically used, although this was occasionally reduced to 4 cm if the measured signal would otherwise be too faint to yield a good curve fit.

The primary goal of these experiments was to assess the accuracy and sensitivity of the estimates of black carbon mass mixing ratio produced by our method. To this end, in Fig. 12 we show a plot of the C_{bc} values estimated with our method versus ground truth estimates obtained using an SP2. Blue data points correspond to the first set of measurements, for which the soot concentrations were relatively low, and red data points correspond to a second set of measurements that was collected after the added black carbon concentration in each snow sample had been approximately doubled.

Upon inspection we see a clear correlation between the estimated and ground truth C_{bc} values. The correlation is approximately linear and nearly one-to-one. Two outlier data points (with ground truth C_{bc} of 58, 59 ppbw) lie off of the one-to-one line. We expect that the outliers are the result of an error in the ground truth estimates. It is possible that our mixing process did not uniformly distribute the black carbon content throughout the snow and that the region sampled for SP2 analysis was unusually clean.

For good measure, we also show the estimates of ice volume fraction, grain radius, and black carbon concentration obtained for the five “double-soot” samples described previously. Estimates are plotted in Fig. 13 as a function of total units of soot-water solution that were applied to each sample using a spray bottle. Although ground truth v_* and r_* were not collected, results in Fig. 13(a) and (b) indicate that the density and grain size of the snow samples was relatively consistent, but did have some variance. This variance may have been caused by differences in how each sample was mixed, or from interaction with the

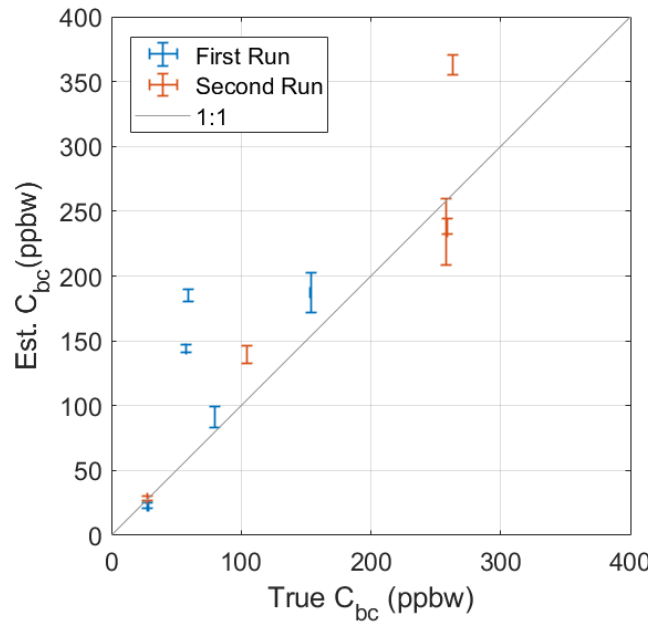


Fig. 12. Retrieved values of black carbon mass mixing ratio C_{bc} plotted with respect to ground truth estimates obtained by a single-particle soot photometer (SP2). Increasing quantities of Sigma-Aldrich fullerene soot were added to five snow samples. Results from the first set of measurements are shown in blue. Soot concentrations were then approximately doubled for all samples and a second set of measurements was taken. Results from the second set of measurements are shown in red. Error bars indicate one standard deviation. SP2 errors are typically too small to be visible.

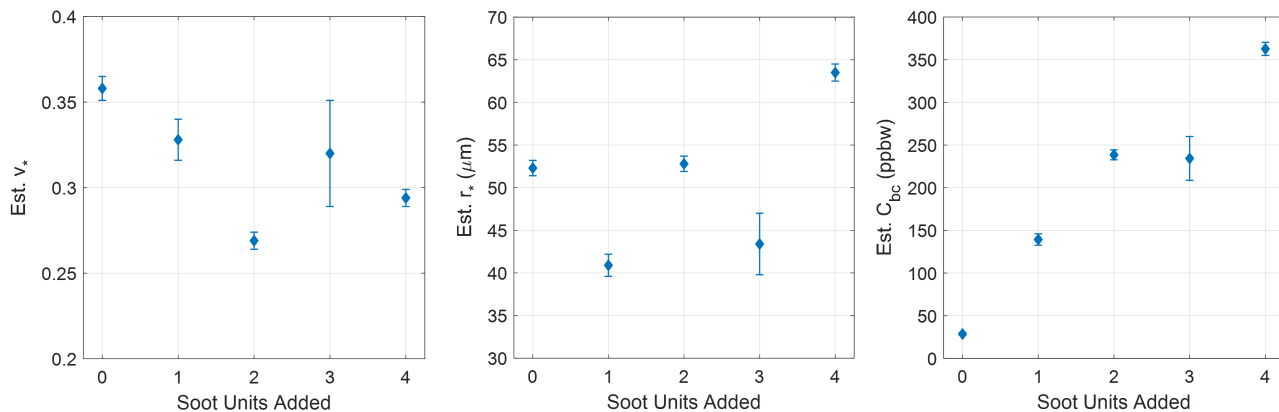


Fig. 13. Estimates of v_* , r_* , and C_{bc} obtained for “double soot” samples. Estimates are plotted as a function of the number of soot units mixed into the snow. One soot unit corresponds to a fixed volume of soot-water suspension that is applied to the snow sample with a spray bottle and then mixed into the snow volume. Error bars indicate one standard deviation.

liquid water in the soot-water suspension. Regardless, we see in Fig. 13(c) that estimated C_{bc} increases approximately linearly and nearly monotonically as a function of the amount of added soot, with no clear dependence on density or grain size.

DISCUSSION

In this work we have introduced a new method for measuring the density, grain size, and black carbon content of a snowpack using non-invasive, time-domain diffuse optical measurements. We have presented a model for the time-domain optical response of a snowpack that was adapted from the biomedical optics literature. Our model was obtained by solving the photon diffusion equation—an approximation to the radiative transfer equation that accurately describes the propagation of light in highly scattering media. We used a Mie scattering model to relate the parameters of our photon diffusion model to snowpack density, grain size, and black carbon concentration, and we developed an algorithm to retrieve these properties from time-domain optical measurements collected at two wavelengths.

We were able to validate our method in a series of proof-of-principle experiments in which we measured the properties of real snow samples using a photon-counting lidar system. The results of these experiments are encouraging. We see a clear, nearly linear correlation between the snowpack densities estimated by our method, and ground truth. When the LAPs in the snow were known to be black carbon particles, we observed a nearly one-to-one correlation between the black carbon mixing ratios estimated using our method, and those measured using a single-particle soot photometer. A correlation was also found between the grain sizes measured by our method and those determined from micro-CT images—although this correlation was not as strong. Our goal in this work was to obtain proof-of-principle results. More experiments are required to comprehensively assess our method’s accuracy, biases, and failure modes.

Although our results are encouraging, we believe that the primary contribution of our work is not necessarily the exact method that we have proposed, but rather that we have been able to clearly demonstrate that time-domain diffuse optics is an appropriate sensing modality for measuring snowpack properties. It is clear from our measurements that the optical response of a snowpack that has been illuminated by a laser pulse can be accurately described using a photon diffusion model. Furthermore, it is clear that this response is measurably influenced by changes to important snowpack properties like grain size, density, and impurity content.

Our method could be improved in many ways. The biases observed in our results suggest that the use of more sophisticated scattering optics models should be explored. Such models might adopt known features of current snowpack albedo models, such as non-spherical grain shapes, but could also consider new physics, such as the effect that internal reflections have on the mean speed of light within the snow. Our measurement procedure could also be improved. In our experiments, processing a single snow sample required between 40 minutes to several hours of data collection time. This could be dramatically reduced by improving our instrument design to incorporate multi-pixel SPAD detectors, higher power lasers, or by simply placing the laser and detector closer to the snow surface. The integration times used in our experiments were also conservative—further analysis could determine the minimum number of photons required to accurately retrieve snow properties. Finally, using our method in the field would require the

development of a rugged and portable instrument. The dramatic decrease in the cost and size of pulsed lasers and photon counting detectors in recent years makes this possible. All components required for such a device can be found in the current model of the iPhone Pro (King and others, 2023).

Although the instrument used in this study was assembled from the same components that make up a typical photon counting lidar system, our measurements were effectively *in situ* because our lidar was always placed within a meter of the snow's surface. In the future, we hope to develop true *remote* lidar sensing techniques that are grounded in time-domain diffuse optics models. Such methods would enable important capabilities such as the remote mapping of snow-water equivalent or impurity concentrations. However the remote sensing environment introduces new challenges that include dramatically lower photon counts, wider beam footprints, and confocal measurement geometries. An alternative direction for future work is the development of more advanced algorithms for processing *in situ* measurements that leverage decades of advances in diffuse optical spectroscopy research. In particular, the adaption of *diffuse optical tomography* methods to snow would enable non-invasive retrieval of snow stratigraphy, or even full 3D mapping of snowpack properties within a probed region. Finally, time-domain optical measurements represent a new opportunity to develop a deeper understanding of the scattering optics of snow. Our work has already shown that, unlike spectral albedo, time-domain diffuse optical signals depend strongly on snowpack density. It's possible that more sophisticated measurements, such as the time-resolved measurement of light penetration or bidirectional reflectance, might be sensitive to other snowpack properties—for example scattering asymmetry, or the absorption enhancement factor—that have been challenging to measure by other means.

ACKNOWLEDGEMENTS

We thank Brent Minchew and Joanna Millstein for the helpful discussions that inspired this project and for support with initial theoretical work. Andrii Murdza provided general assistance with micro-CT measurements and cold room experiments. Anna Valentine prepared the snow samples used in our soot addition experiments. Jacob Chalif ran our SP2 measurements and helped us interpret the results. Connor Henley was supported by a Draper Scholarship and by a grant from the Office of Naval Research (N00014-21-C-1040). Any opinions, findings and conclusions or recommendations expressed in this material are those of the author(s) and do not necessarily reflect the views of the Office of Naval Research. Colin R. Meyer was supported by the Heising-Simons Foundation (#2020-1911), the Army Research Office (78811EG), and the National Science Foundation (2024132).

REFERENCES

Ackermann M and others (2006) Optical properties of deep glacial ice at the south pole. *Journal of Geophysical Research: Atmospheres*, **111**(D13) (doi: <https://doi.org/10.1029/2005JD006687>)

Allgaier M and Smith BJ (2022) Smartphone-based measurements of the optical properties of snow. *Appl. Opt.*, **61**(15), 4429–4436 (doi: 10.1364/AO.457976)

Allgaier M, Cooper MG, Carlson AE, Cooley SW, Ryan JC and Smith BJ (2022) Direct measurement of optical

properties of glacier ice using a photon-counting diffuse lidar. *Journal of Glaciology*, **68**(272), 1210–1220 (doi: 10.1017/jog.2022.34)

Bentley W and Humphreys W (1931) *Snow Crystals*. McGraw-Hill, New York, NY

Doherty SJ, Dang C, Hegg DA, Zhang R and Warren SG (2014) Black carbon and other light-absorbing particles in snow of central north america. *Journal of Geophysical Research: Atmospheres*, **119**(22), 12,807–12,831 (doi: <https://doi.org/10.1002/2014JD022350>)

Durduran T, Choe R, Baker W and Yodh A (2010) Diffuse optics for tissue monitoring and tomography. *Reports on progress in physics*, **73**(7), 076701

Fair Z, Flanner M, Vuyovich C, Adam MS and others (2022) Quantifying volumetric scattering bias in icesat-2 and operation icebridge altimetry over snow-covered surfaces. *Authorea Preprints*

Fierz C, Armstrong R, Durand Y, Etchevers P, Greene E, McClung D, Nishimura K, Satyawali P and Sokratov S (2009) The international classification for seasonal snow on the ground, the international classification for seasonal snow on the ground, ihp-vii technical documents in hydrology no 83, iacs contribution no 1

Flanner MG, Arnheim JB, Cook JM, Dang C, He C, Huang X, Singh D, Skiles SM, Whicker CA and Zender CS (2021) Snicar-adv3: a community tool for modeling spectral snow albedo. *Geoscientific Model Development*, **14**(12), 7673–7704 (doi: 10.5194/gmd-14-7673-2021)

Gallet JC, Domine F, Zender CS and Picard G (2009) Measurement of the specific surface area of snow using infrared reflectance in an integrating sphere at 1310 and 1550 nm. *The Cryosphere*, **3**(2), 167–182 (doi: 10.5194/tc-3-167-2009)

Grenfell TC, Doherty SJ, Clarke AD and Warren SG (2011) Light absorption from particulate impurities in snow and ice determined by spectrophotometric analysis of filters. *Appl. Opt.*, **50**(14), 2037–2048 (doi: 10.1364/AO.50.002037)

Hagenmuller P, Matzl M, Chambon G and Schneebeli M (2016) Sensitivity of snow density and specific surface area measured by microtomography to different image processing algorithms. *The Cryosphere*, **10**(3), 1039–1054 (doi: 10.5194/tc-10-1039-2016)

Haskell RC, Svaasand LO, Tsay TT, Feng TC, McAdams MS and Tromberg BJ (1994) Boundary conditions for the diffusion equation in radiative transfer. *J. Opt. Soc. Am. A*, **11**(10), 2727–2741 (doi: 10.1364/JOSAA.11.002727)

Henderson GR, Peings Y, Furtado JC and Kushner PJ (2018) Snow–atmosphere coupling in the northern hemisphere. *Nature Climate Change*, **8**(11), 954–963 (doi: 10.1038/s41558-018-0295-6)

Henley C (2020) Snow lidar monte-carlo simulator. Available at <https://github.com/co24401/SnowLiDARMonteCarlo>

Kienle A and Patterson MS (1997) Improved solutions of the steady-state and the time-resolved diffusion equations for reflectance from a semi-infinite turbid medium. *J. Opt. Soc. Am. A*, **14**(1), 246–254 (doi: 10.1364/JOSAA.14.000246)

King F, Kelly R and Fletcher CG (2023) New opportunities for low-cost lidar-derived snow depth estimates from a consumer drone-mounted smartphone. *Cold Regions Science and Technology*, **207**, 103757, ISSN 0165-232X (doi: <https://doi.org/10.1016/j.coldregions.2022.103757>)

Kokhanovsky AA and Zege EP (2004) Scattering optics of snow. *Appl. Opt.*, **43**(7), 1589–1602 (doi: 10.1364/AO.43.001589)

Lazarcik J, Dibb JE, Adolph AC, Amante JM, Wake CP, Scheuer E, Mineau MM and Albert MR (2017) Major fraction of black carbon is flushed from the melting new hampshire snowpack nearly as quickly as soluble impurities. *Journal of Geophysical Research: Atmospheres*, **122**(1), 537–553 (doi: <https://doi.org/10.1002/2016JD025351>)

Li C, Grobmyer SR, Massol N, Liang X, Zhang Q, Chen L, Fajardo LL and Jiang H (2008) Noninvasive in vivo tomographic optical imaging of cellular morphology in the breast: Possible convergence of microscopic pathology and macroscopic radiology. *Medical Physics*, **35**(6Part1), 2493–2501

Libois Q, Picard G, France JL, Arnaud L, Dumont M, Carmagnola CM and King MD (2013) Influence of grain shape on light penetration in snow. *The Cryosphere*, **7**(6), 1803–1818 (doi: 10.5194/tc-7-1803-2013)

Libois Q, Picard G, Dumont M, Arnaud L, Sergent C, Pougatch E, Sudul M and Vial D (2014) Experimental determination of the absorption enhancement parameter of snow. *Journal of Glaciology*, **60**(222), 714–724 (doi: 10.3189/2014JoG14J015)

McCullagh P (2019) *Generalized linear models*. Routledge

Nolin A and Dozier J (2000) A hyperspectral method for remotely sensing the grain size of snow. *Remote sensing of Environment*, **74**(2), 207–216

Painter TH, Deems JS, Belnap J, Hamlet AF, Landry CC and Udall B (2010) Response of colorado river runoff to dust radiative forcing in snow. *Proceedings of the National Academy of Sciences*, **107**(40), 17125–17130 (doi: 10.1073/pnas.0913139107)

Painter TH, Bryant AC and Skiles SM (2012) Radiative forcing by light absorbing impurities in snow from modis surface reflectance data. *Geophysical Research Letters*, **39**(17) (doi: <https://doi.org/10.1029/2012GL052457>)

Quarto G, Spinelli L, Pifferi A, Torricelli A, Cubeddu R, Abbate F, Balestreri N, Menna S, Cassano E and Taroni P (2014) Estimate of tissue composition in malignant and benign breast lesions by time-domain optical mammography. *Biomed. Opt. Express*, **5**(10), 3684–3698 (doi: 10.1364/BOE.5.003684)

Robledano A, Picard G, Dumont M, Flin F, Arnaud L and Libois Q (2023) Unraveling the optical shape of snow. *Nature Communications*, **14**(1), 3955 (doi: 10.1038/s41467-023-39671-3)

Satat G (2019) *All photons imaging : time-resolved computational imaging through scattering for vehicles and medical applications with probabilistic and data-driven algorithms*. Ph.D. thesis, Massachusetts Institute of Technology, Cambridge, MA

Sevick E, Chance B, Leigh J, Nioka S and Maris M (1991) Quantitation of time- and frequency-resolved optical spectra for the determination of tissue oxygenation. *Analytical Biochemistry*, **195**(2), 330–351, ISSN 0003-2697 (doi: [https://doi.org/10.1016/0003-2697\(91\)90339-U](https://doi.org/10.1016/0003-2697(91)90339-U))

Skiles S, Flanner M, Cook J, Dumont M and Painter T (2018) Radiative forcing by light-absorbing particles in snow. *Nature Clim. Change*, **8**(11), 964–971

Smith BE, Gardner A, Schneider A and Flanner M (2018) Modeling biases in laser-altimetry measurements caused by scattering of green light in snow. *Remote Sensing of Environment*, **215**, 398–410 (doi: <https://doi.org/10.1016/j.rse.2018.06.012>)

Sumlin BJ, Heinson WR and Chakrabarty RK (2018) Retrieving the aerosol complex refractive index using pymiemscatt: A mie computational package with visualization capabilities. *Journal of Quantitative Spectroscopy and Radiative Transfer*, **205**, 127–134 (doi: <https://doi.org/10.1016/j.jqsrt.2017.10.012>)

Várnai T and Cahalan RF (2007) Potential for airborne offbeam lidar measurements of snow and sea ice thickness. *Journal of Geophysical Research: Oceans*, **112**(C12) (doi: <https://doi.org/10.1029/2007JC004091>)

Warren SG (2019) Optical properties of ice and snow. *Philosophical Transactions of the Royal Society A: Mathematical, Physical and Engineering Sciences*, **377**(2146), 20180161 (doi: [10.1098/rsta.2018.0161](https://doi.org/10.1098/rsta.2018.0161))

Warren SG and Brandt RE (2008) Optical constants of ice from the ultraviolet to the microwave: A revised compilation. *Journal of Geophysical Research*, **113**(D14)

Welch AJ and van Gemert MJ (1995) *Optical-thermal response of laser-irradiated tissue*. Springer, New York

Wiscombe WJ and Warren SG (1980a) A model for the spectral albedo of snow. i: Pure snow. *Journal of Atmospheric Sciences*, **37**, 2712–2733

Wiscombe WJ and Warren SG (1980b) A model for the spectral albedo of snow. ii: Snow containing atmospheric aerosols. *Journal of Atmospheric Sciences*, **37**(12), 2735–2745

Zappa F, Tisa S, Tosi A and Cova S (2007) Principles and features of single-photon avalanche diode arrays. *Sensors and Actuators A: Physical*, **140**(1), 103–112, ISSN 0924-4247 (doi: <https://doi.org/10.1016/j.sna.2007.06.021>)

Zege E, Katsev I, Malinka A, Prikhach A, Heygster G and Wiebe H (2011) Algorithm for retrieval of the effective snow grain size and pollution amount from satellite measurements. *Remote Sensing of Environment*, **115**(10), 2674–2685, ISSN 0034-4257 (doi: <https://doi.org/10.1016/j.rse.2011.06.001>)